VOL. 16, NO. 24, DECEMBER 2021 ISSN 1819-6608
ARPN Journal of Engineering and Applied Sciences

www.arpnjournals.com

SELIG AIRFOILS: TOPOLOGY OF FLOW PATTERNS AT LOW REYNOLDS NUMBER

Che Intan Hartini Che Ibrahim and Aslam Abdullah
Department of Aeronautical Engineering, Faculty of Mechanical and Manufacturing Engineering,
Universiti Tun Hussein Onn Malaysia, Parit Raja, Batu Pahat, Johor, Malaysia
E-Mail: aslam@uthm.edu.my

ABSTRACT

Over the years, extensive discussions on the flow topology have sparked a motivation for deeper studies on the process of vortex formation and the periodic behaviour of the reattachment profile. Despite a clear methodology, such flow topology studies have not yet covered the majority of airfoil types. This study considers three low Reynolds number Selig airfoils. The computational fluid dynamics simulations carried out involve the airflow passing these models. The attention is given mainly on the separation bubble, vortex shedding and reattachment point. The corresponding effects on airfoils aerodynamic performance are observed. The method is validated against an established mathematical relationship to indicate that both simulations and analysis technique are reliable. The results are applicable in micro aerial vehicles field where the airfoils are those of low Reynolds number.

Keywords: topology of flow patterns, Selig airfoils, vortex shedding, separation bubble, reattachment point.

1. INTRODUCTION

Singular fixed points are used in analysing flow topology to understand the physics of flow and its complex structure. The topology concerns the structures within the flow field [1, 4] such as separation bubble and shedding of vortices. The construction of mathematical model in diagnosing the critical air loads can be analysed by obtaining the information of topologic bifurcation via flow topology [3, 5]. Flow topology therefore is important if we are to perform deeper insight of, for instance, available analysis of flow past airfoils [6, 7], and even more specific problems involving the ground effects or wind turbine drag coefficient [8, 9].

The developed oscillating flow induces the vortex shedding which grows and moves before it is able to detach from the surface of the airfoil at the trailing edge. The formation and shedding of the vortices and the encased bubble between the point of separation and reattachment point on the surface of the airfoil (i.e. separation bubble) significantly affect the aerodynamic performance of airfoils [10]. Failure of the separated flow to reattach to the surface of airfoil will lead to stall condition or loss of lift.

The formation of separation bubble on the surface of airfoil can be longer at low Reynolds number regime, until it reaches complete flow separation leading to stall condition [11]. Hence, the design and geometry of low Reynolds number airfoils can reduce the risk of the complete separation in the application of, for instance, micro aerial vehicle (MAV).

The study considers three low Reynolds number airfoils from series of Selig (i.e. S3021, S3024, S3025). It highlights the formation and development of separation bubble and vortex shedding, and their relations to the lift and drag coefficients, by using the method of singular fixed point.

It is the aim of the study to understand the phenomena of vortex shedding and separation bubble effects on the airfoils' aerodynamic performance.

2. LOW REYNOLDS NUMBER AIRFOILS

Illustrated in Figure-1 is the geometry of the low Reynolds number airfoils. Respective grid, computational domain and boundary conditions are shown in Figure-2.

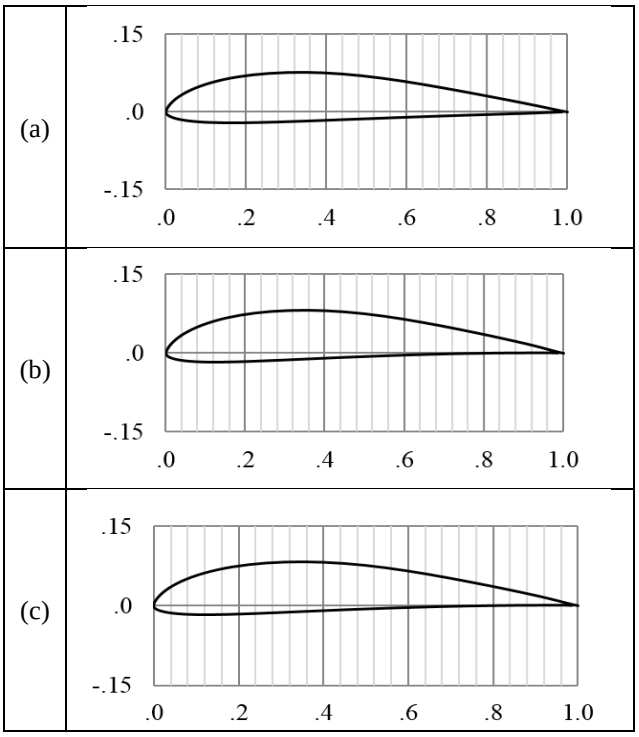

Figure-1. Geometry of low Reynolds number airfoils (a) S3021 (b) S3024 (c) S3025.

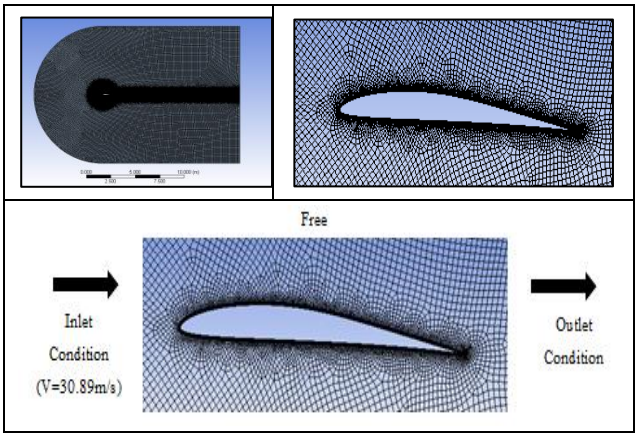

Figure-2. Grid, domain and boundary conditions.

3. TOPOLOGICAL OVERVIEW

Both vortex shedding and separation bubble profile information are gained in this study by means of the topological overview of the flow. It has been proven that the model of laminar is useful in yielding better result for observing flow topology with vortex shedding [5, 12]. The flow development involves the velocity curl profile over the airfoils in fixed laminar condition, with respect to time. In this simulation, two-dimensional flows over a set of airfoils (i.e. Selig airfoils) are examined. The free stream velocity is 30.89 ms^{-1} and the Reynolds number is Re = 60 000. These wing types are applicable for MAVs and Re = 60 000 is in the typical range of MAV operation [3]. The chord length of each airfoil is set as 1 meter. A time step of t = 0.0015-unit time is used for accuracy, but to conserve memory only every 8thtime step is stored. Therefore, the time step for the exported data files is t = 0.012 time units. In this simulation, 600 velocity time steps were analyzed, for $\alpha = 4^{\circ}$. The Cartesian mesh covers the domain $-7\text{ m} \le x \le 14\text{ m}$, $-7\text{ m} \le y \le 7\text{ m}$, with the initial grid spacing of $\Delta x = \Delta y = 0.02$ m. This grid spacing is necessary to capture the fine detailed structures in the wake region and to ensure the accuracy of the manifold calculations. The accurate calculation of Lagrangian coherent structures requires that the grid spacing be small [3]. The transition time is set to Δt = 0.012unit time to optimize the appearance of the desired flow structures. Longer transition times lead to the loss of important features while shorter transition times fail to reveal the desired level of detail.

Each flow is simulated at 4ºairfoils angle of attack and Reynolds number of 60,000 with a CFD software. In general, 'proximity and curvature' size function, fine relevance center, and maximum face size of 0.1 m are chosen. Type of body sizing is '(two) body of influence' with element and size growth rate of 0.02 m and 1.2, respectively, and '1 body' geometry selection. 'Edge sizing 1' type is 'number of (250) divisions', with sizing behaviour and the geometry are set to be hard and consists of 2 edges, respectively. Edge sizing 2 type is also 'number of (5) divisions', with sizing behaviour is set to be hard for '1 edge' geometry. The selected options for inflation technique are '1 face' geometry, '3 edges' boundary, and inflation of 'total thickness' type with 10 layers, 1.2 growth rate, and 0.01 m maximum thickness.

The setup includes density based solver, absolute velocity formulation, transient condition and planar 2D space, in general. Laminar model is used, while energy equation model is not considered. Constant air density and viscosity values are 1.225 kg/m^3 and 1.7894 x 10^{-05} kg/m.s, respectively. Boundary conditions include no slip wall condition, inlet velocity, 'magnitude and direction' velocity specification method, absolute reference frame, zero initial gauge pressure, and component x-y = (1,0) of flow direction. Outlet type is that of 'pressure-outlet', where absolute backflow reference frame, zero pressure gauge, and 'normal to boundary' backflow direction specification method, are employed. The solution method is that of implicit, with Roe Flux-Difference Splitting scheme, spatial discretization of least squares cell based and second order upwind for estimating spatial gradient and flow, respectively. The transient formulation is that of second order implicit. In the solution initialization process, we set standard initialization method which computes from inlet, with the reference frame that is relative to cell zone, initial non-zero velocity value only as x-component, and initial zero-gauge pressure.

Every 8 time steps, the calculation activities are auto saved. Fixed time stepping method is applied, with 600 number of time steps, the maximum of 3700 iterations per reporting interval, and a single profile update interval.

4. FLOW TOPOLOGY AROUND S3024

It is found that, in the case of S3024, the reverse saddle-node bifurcation as well as shedding of vortex take place at t_2 and t_3, respectively. The flow topology is given in Figure-3 with respect to three different times. The dash lines represent the boundaries of the segment in which singular fixed points are located. All types of fixed point at t_1, t_2, and t_3 are validated against Hunt relationship. Table-1 shows the finding summary based on such relationship.

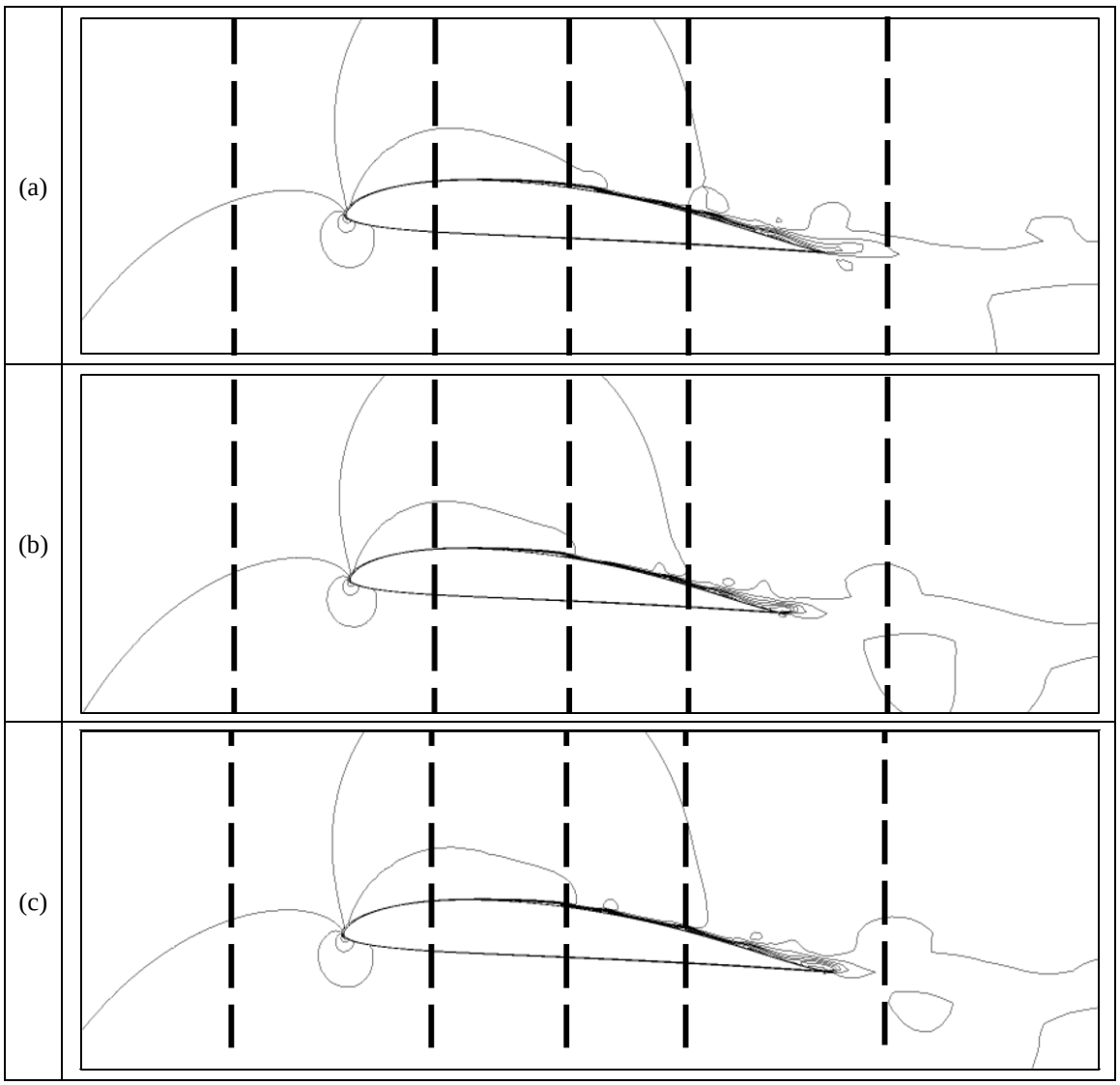

Figure-3. Flow topology aroundS3024 with Re = 60,000 at α = 4ºat time(a) t_1(b) t_2 (c) t_3.

Table-1. Summary of topological fixed points in the flow over SeligS3024.

Segment	Four-Way Elliptic Fixed Points (E)	Three-Way Elliptic Fixed Points (E')	Four-Way Hyperbolic Fixed Points (H)	Three-Way Hyperbolic Fixed Points (H')
t_1	8	0	5	8
t_2	8	0	5	8
t_3	9	0	5	10

Segment 1 captures no significant event at each time of interest. It can be seen at t_1 to $t_2$of the flow topology in segment 2 (see Figure-4), that an elliptic fixed points, E1, and those of hyperbolic, H1 and H2, move toward the rear of the separation bubble. The movement causes the collision between E1 and a newly formed hyperbolic fixed point resulting from the collision of H1 and H2. The collision between the elliptic and the hyperbolic fixed points lead to occurrence of reverse saddle-node bifurcation, where they destroy each other and separate a new vortex from the separation bubble.

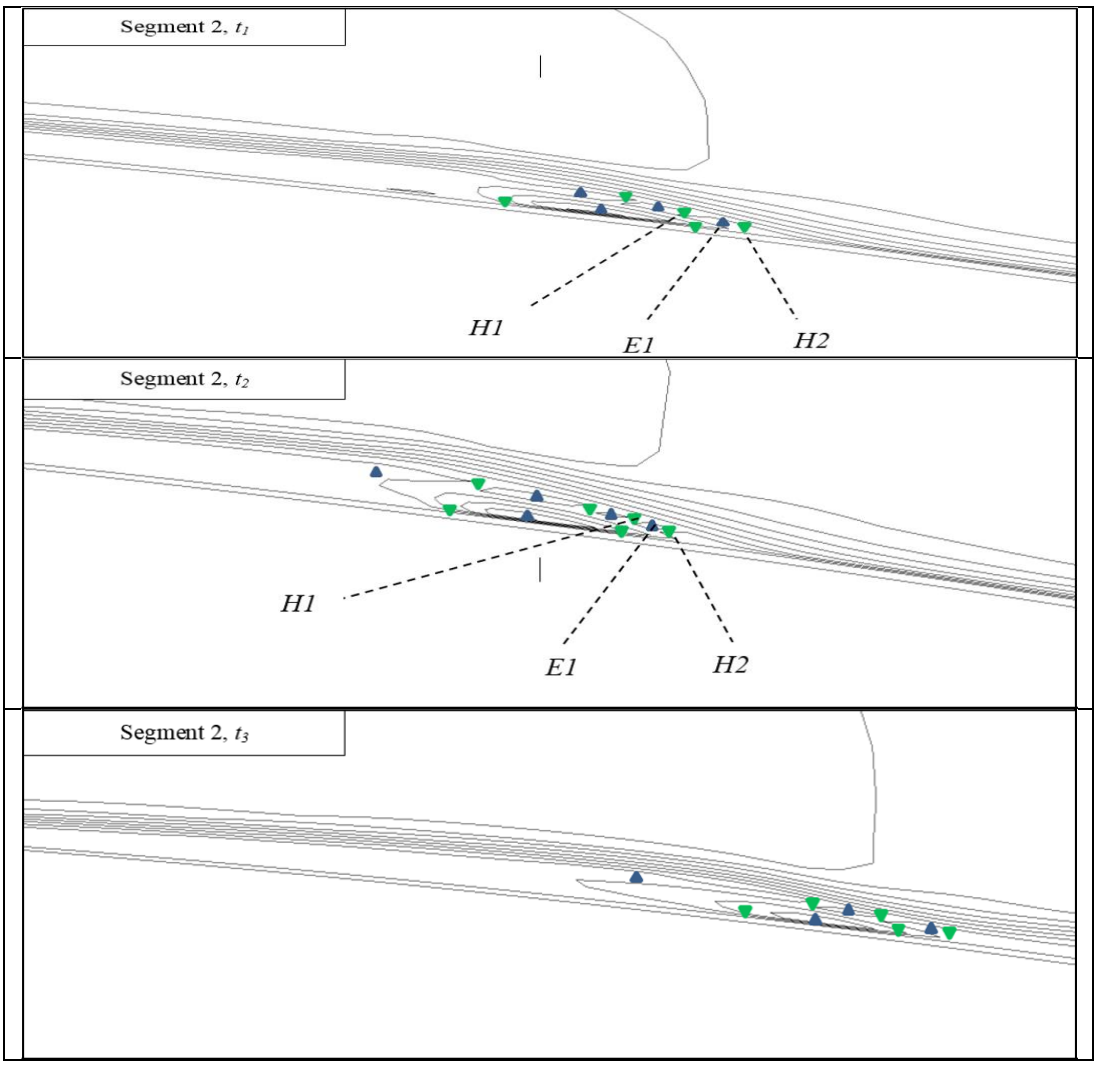

Figure-4. Segmented flow topology (segment 2) around S3024 with *Re* = 60,000 at $\alpha = 4^o$.

Segment 3 reveals the movement and the change of the topological fixed points before the vortex is ready to be shed in segment 4 (see Figure-5). At $t_2$and t_3 in segment 4, three-way hyperbolic points collide with each other; H3 and H5 collide with H4 and H6, respectively, as they move towards the rear of the airfoil until they get separated from the airfoil surface. For this airfoil, the occurrence of vortex shedding cannot be directly observed at the selected times (i.e. at t_1, t_2, and t_3). However, the prediction can be made as the vortices are nearly shed at the trailing edge and by observing the movement of the fixed points.

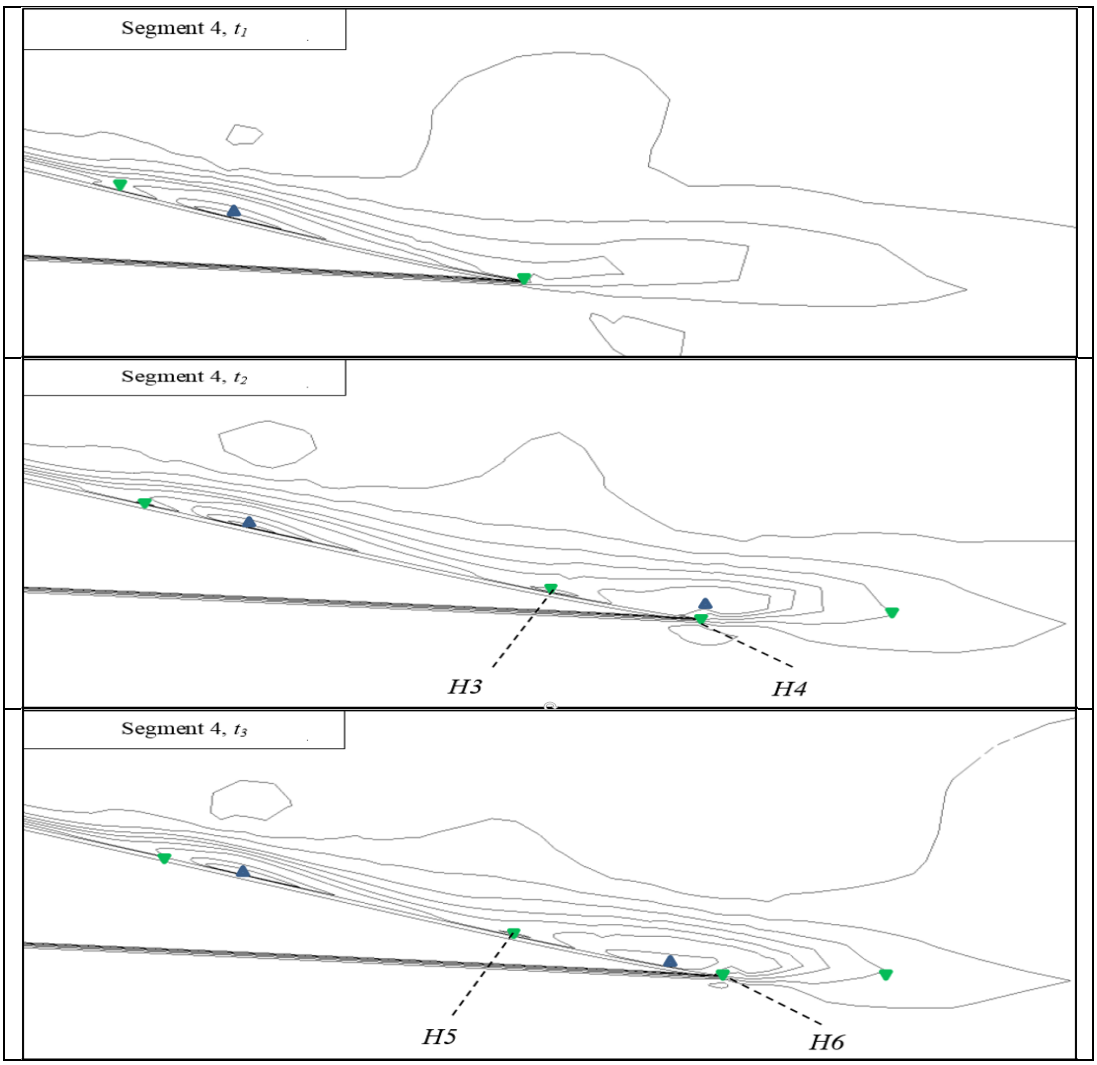

Figure-5. Segmented flow topology (segment 4) around S3024 with *Re* = 60,000 at α = 4º.

Segment 5 focuses on the downstream of the airfoil which is beyond the scope of the study.

The values in Table-1 are substituted in equation

$$\left(\sum E + \frac{1}{2}\sum E'\right) - \left(\sum H + \frac{1}{2}\sum H'\right) = 1 - n \quad (1)$$

where n = 2 for all t_1, t_2, and t_3. The results of lift and drag are shown in Table-2.

Table-2. Values of c_l and c_d.

Time	c_l	c_d
t_1	7.7862×10^{-1}	8.0568×10^{-3}
t_2	7.4386×10^{-1}	1.2058×10^{-3}
t_3	7.9787×10^{-1}	7.3116×10^{-3}

The highest lift is obtained at t_3 where its coefficient $c_l = 7.9787 \times 10^{-1}$, while the lowest lift coefficient is found at t_2 where $c_l = 7.4386\times10^{-1}$. The lift is the highest at $t_3$due relatively shorter reattachment length in comparison to that at t_1. Moreover, the vortex shedding negatively affects the lift of the airfoil at t_2. However, the drag is the lowest at t_2. The reason is that at $t_2$the separation bubble is the thickest.

5. FLOW TOPOLOGYAROUNDS3025

In the case S3025, the reverse saddle-node bifurcation occurs at t_2 while shedding of vortex occurs att_3. The number of each type of fixed points at three different time as shown in Table-3 is confirmed by Hunt relationship.

As in the previous case (i.e. that of S3024), segment 1 reveals no occurrence at every time of interest. Based on the flow topology at t_1 to $t_2$in segment 2 as shown by Figure-6, an elliptic fixed point, E1, and those of hyperbolic, H1 and H2, move toward the rear of the separation bubble, causing the collision between E1 and a newly formed hyperbolic fixed point (i.e. that resulting from collision of H1 and H2). The collision between these fixed points leads to reverse saddle-node bifurcation, the situation in which the points eliminate each other and split the separation bubble to form a new vortex. Note that H1, H2 and E1 can be observed as earlier as at t_1.

Table-3. Summary of topological fixed points in the flow over Selig S3025.

Segment	Four-Way Elliptic Fixed Points (E)	Three-Way Elliptic Fixed Points (E')	Four-Way Hyperbolic Fixed Points (H)	Three-Way Hyperbolic Fixed Points (H')
t_1	7	0	4	8
t_2	5	0	1	10
t_3	8	0	5	8

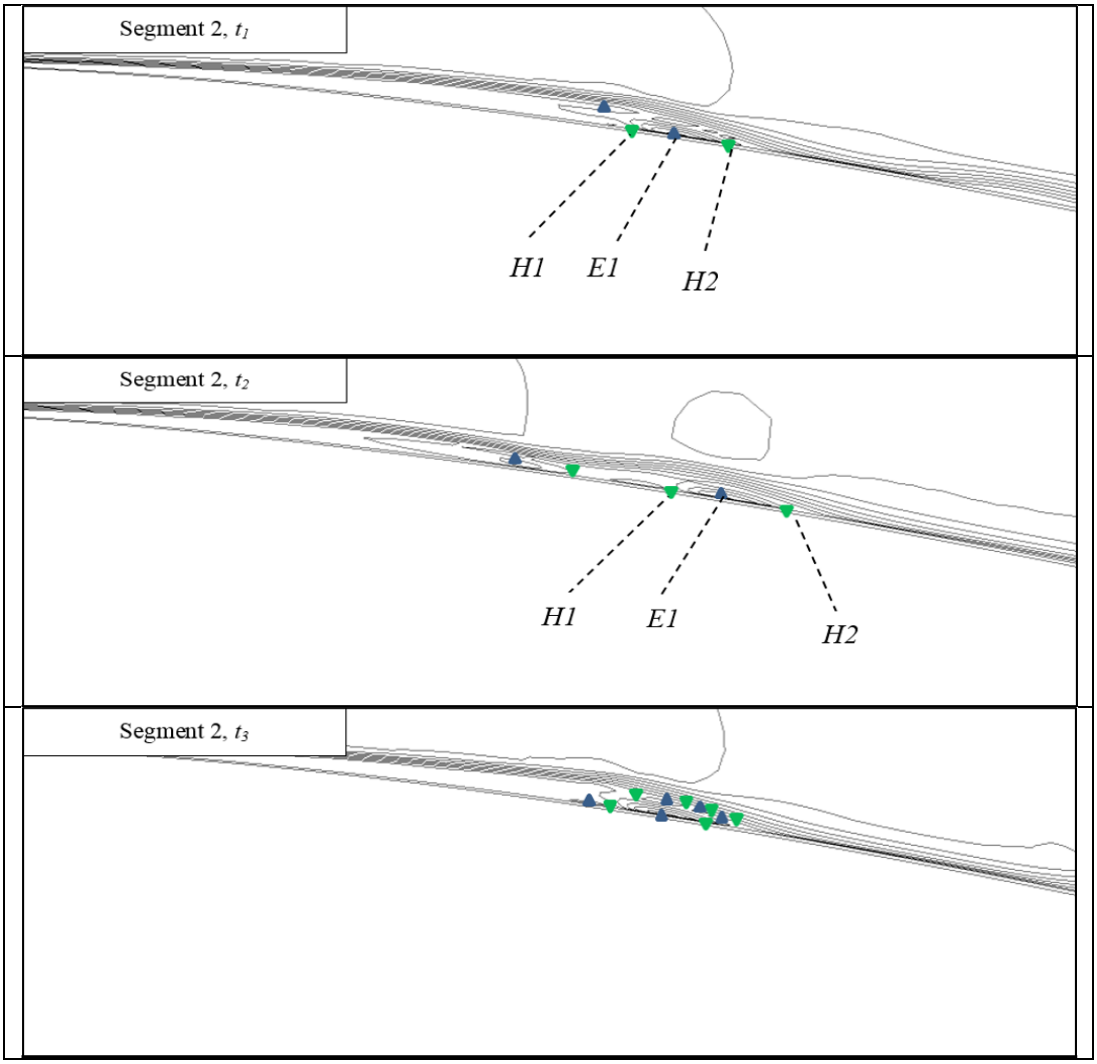

Figure-6. Segmented flow topology (segment 2) around S3025 with Re = 60,000 at α = 4°.

The separation bubble's movement is captured in segment 3. In segment 4 at t_3, as shown by Figure-7, two three-way hyperbolic points, namely H3 and H4 will collide as they move toward the rear of the airfoil and finally completely detach from its surface. This creates a new four-way hyperbolic point just below the shed vortex.

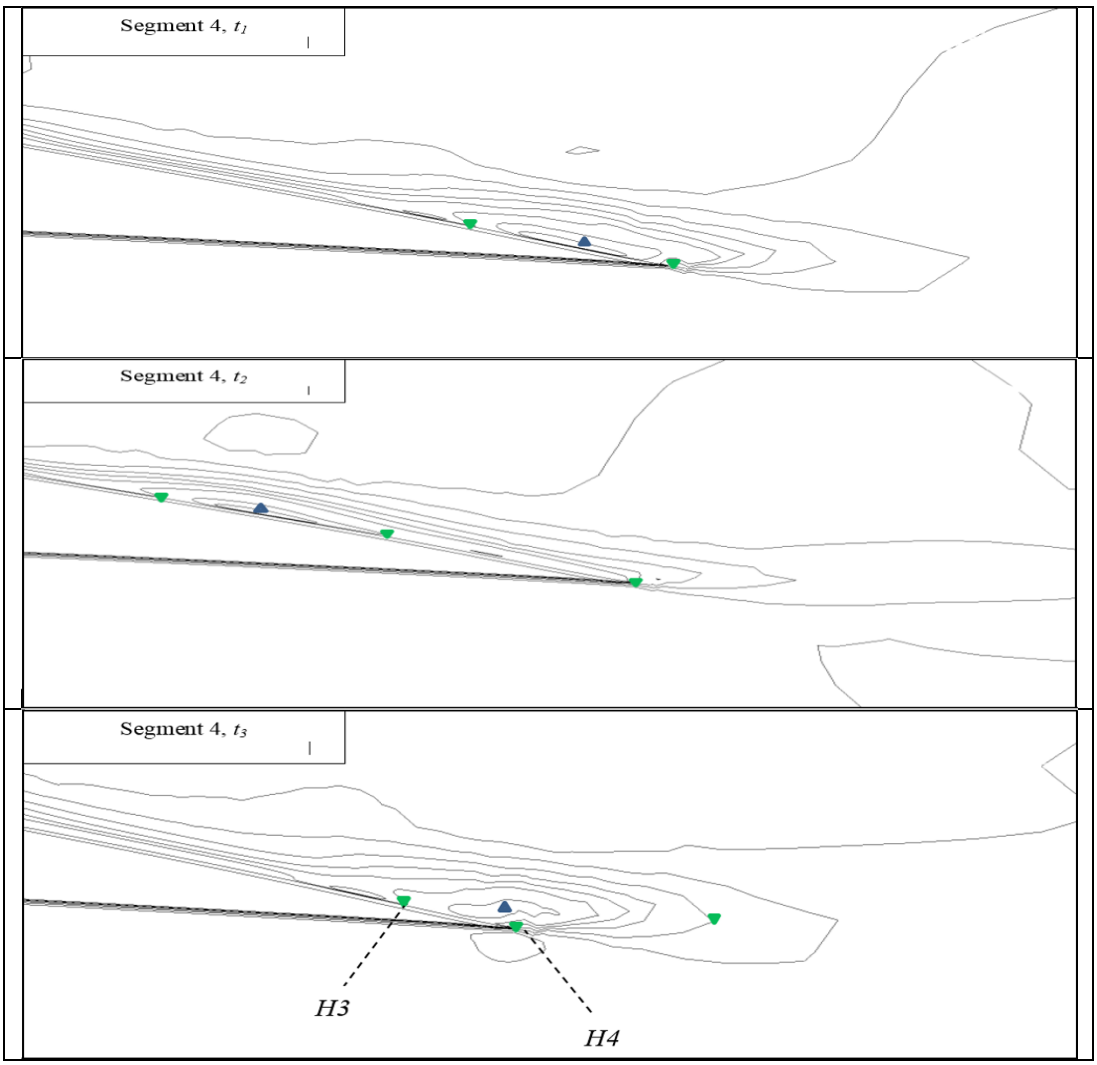

Figure-7. Segmented flow topology (segment 4) around S3025 with *Re* = 60,000 at α = 4°.

Substituting the values in Table-3 into (1), we find that $n = 2$ is true for t_1, t_2, andt_3. The list of c_l and c_d values with respect to time is given in Table-4.

Table-4. Values of c_l and c_d.

Time	c_l	c_d
t_1	8.1121×10^{-1}	1.1146×10^{-2}
t_2	8.3160×10^{-1}	1.4404×10^{-2}
t_3	7.5115×10^{-1}	2.2434×10^{-2}

At t_2, the lift coefficient $c_l = 8.3160 \times 10^{-1}$ which is the largest while at t_3, $c_l = 7.5115 \times 10^{-1}$ which is the smallest.

At t_2, the separation bubble is the thinnest in comparison to that at t_1 and t_3. At t_3, the number of vortices in the separation bubble is maximum which indirectly increases its thickness, and the vortex is shed, which in turn degrade the lift significantly. Note that the vortex shedding also occurs in between t_1 and t_2. Clearly, the vortex shedding negatively affects the lift.

There is no significant activity in segment 1. At t_2 in segment 2, it can be seen that points E1, H1 and H2 move towards the rear of the separation bubble. Consequently, H1 and H2 destroy each other in a collision that marks the occurrence of reverse saddle-node bifurcation. This results in the splitting of the separation bubble to produce a new fixed hyperbolic point

6. FLOW TOPOLOGYAROUNDS3021

The reverse saddle-node bifurcation and vortex shedding occur at $t_2$and t_3, respectively. Table-5 shows the number of each singular fixed point type whose validity needs to be validated against Hunt relationship.

Table-5. Summary of topological fixed points in the flow over S3021.

Segment	Four-Way Elliptic Fixed Points (E)	Three-Way Elliptic Fixed Points (E')	Four-Way Hyperbolic Fixed Points (H)	Three-Way Hyperbolic Fixed Points (H')
t_1	5	0	1	8
t_2	6	0	3	6
t_3	5	0	2	6

The tabulated c_l and c_d with respect to time of interests are shown in Table-6.

Table-6. Values of c_l and c_d.

Time	c_l	c_d
t_1	6.6406×10^{-1}	2.7324×10^{-3}
t_2	6.9714×10^{-1}	8.1822×10^{-3}
t_3	6.7221×10^{-1}	5.3508×10^{-3}

The highest lift is observed at t_2 where $c_l = 6.9714 \times 10^{-1}$. At this time, the reattachment length is the shortest and there is no occurrence of vortex shedding (see Figure-8). However, the separation bubble at $t_2$is the thickest, resulting a bump which disturbs the airflow and negatively affects the drag (i.e. the drag increases). The separation bubble then gets thinner at t_3 when the reverse saddle-node bifurcation takes place and splits the separation bubble to produce a new vortex.

The smallest lift with $c_l = 6.6406 \times 10^{-1}$ is found at t_1 when the reattachment length is the maximum.

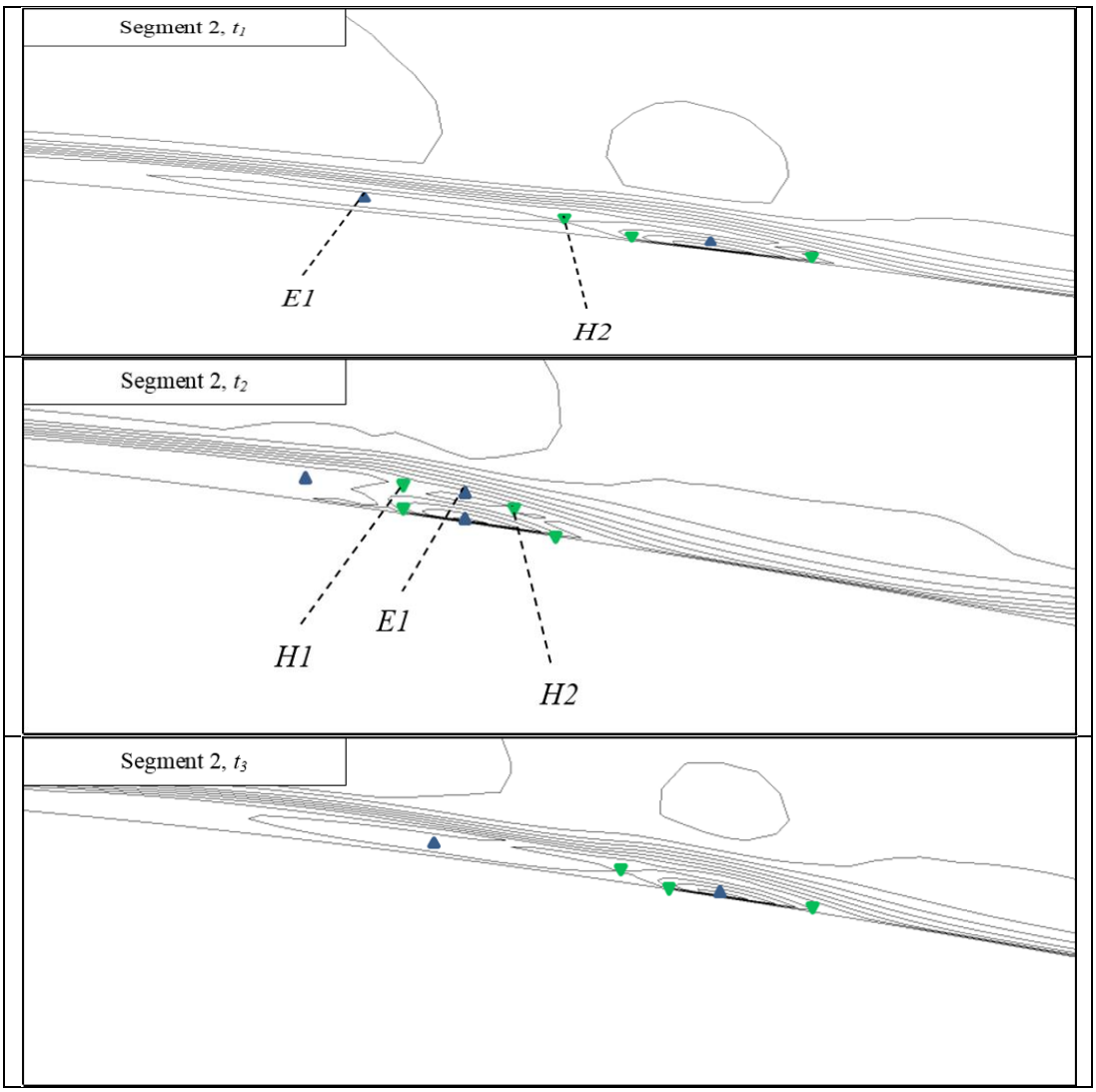

Figure-8. Segmented flow topology (segment 2) around S3021 with Re = 60,000 at α = 4°.

The developing vortices towards the trailing edge from t_1 to t_3 is captured in segment 3. At t_3 (Segment 4) three-way hyperbolic points, namely H2 and H3 collide each other as they move towards the airfoil's rear, and then separate from the airfoil surface (see Figure-9). Theoretically, the collision creates a new four-way hyperbolic point located right below the shed vortex.

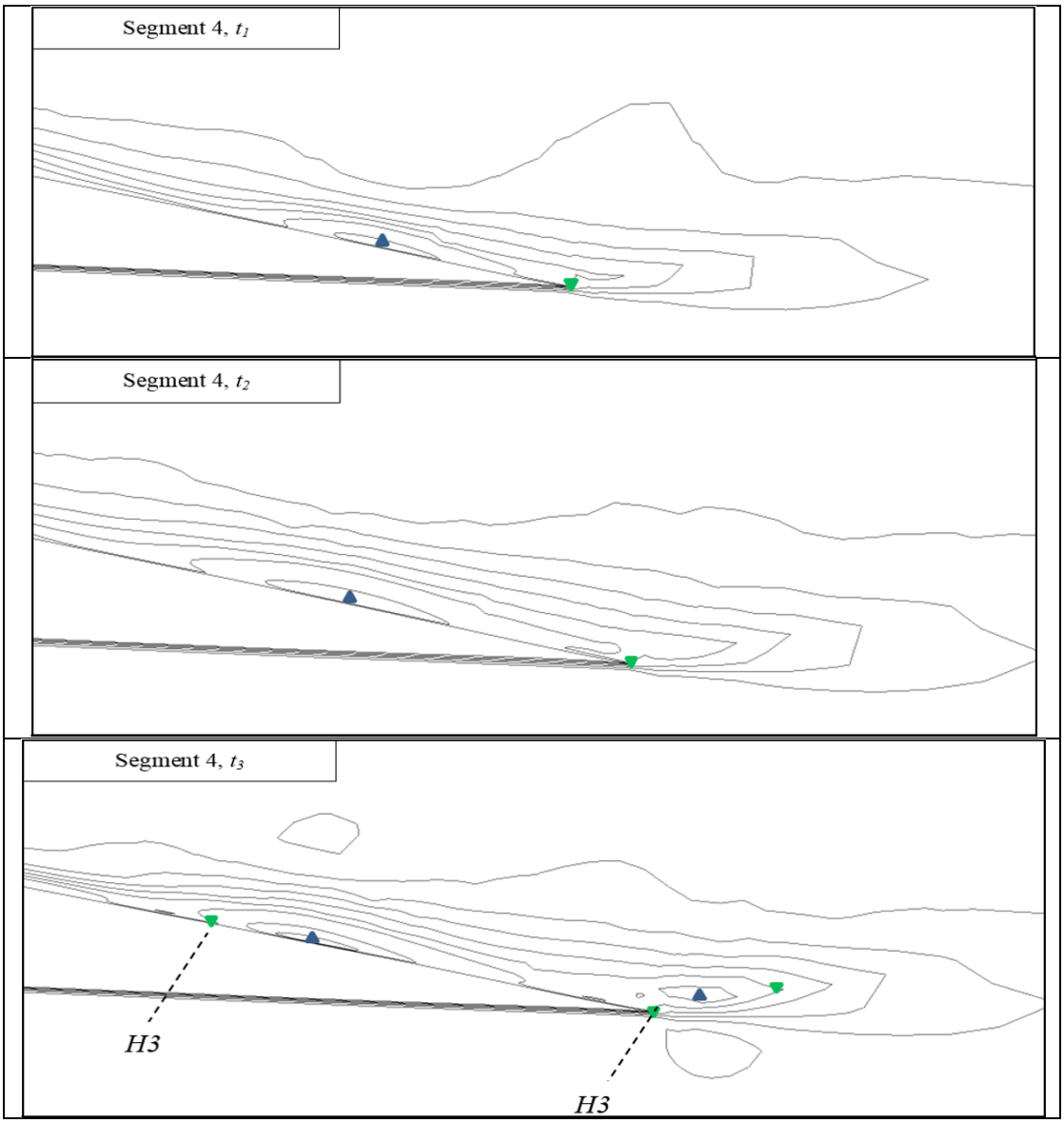

Figure-9. Segmented flow topology (segment 4) around S3021 with *Re* = 60,000 at α = 4°.

When substituting the values in Table-5into (1), we consistently have n = 1 for all time of interests.

7. FINAL REMARKS

There are several points which are worth to note in the application of micro aerial vehicle, based on the simulation and analysis of the flow over low Reynolds number Seligairfoils. These airfoils are designed in such a way that the possibility of the flow separation is minimized in order to prevent the drop in lift. Canonical airfoils have higher tendency to experience complete flow separation when operate in low Reynolds number regime.

The presence of separation bubble on the airfoil's surface disturbs the airflow around the surface. The velocity of air decreases when the air passes the bubble thus causes the rise in pressure that might lead to boundary layer separation. The highly sensitive boundary layer is originally in tangential direction to the surface, but can be easily affected by any disturbance as the separation bubble. When such disturbance leads to instability, then the laminar flow would become turbulence which is a state unfavourable to any flying device. Low Reynolds number airfoils (e.g. Selig airfoils) have a good characteristic to reattach the streamlines to the airfoil surface while passing the separation bubble, thus preventing the transition to turbulent flow.

In the case where the separation bubble cannot be avoided, it needs to contain as few vortices and to be as

thin as possible in order to reduce the risk of complete flow separation. Relatively thicker separation bubble which might be associated to more vortices it contains degrades the lift and increases the drag.

The vortex shedding also directly reduces the lift and increases the drag. Itis one of the unfavourable conditions in flying machines yet cannot be fully eradicated. Giving the right technique, however, its effects can be minimized.

ACKNOWLEDGEMENT

The authors would like to thank Universiti Tun Hussein Onn Malaysia (UTHM) and Ministry of Higher Education Malaysia (MoHE) for the research facilities.

REFERENCES

[1] Perry A. E. and Chong M.S.1994. Topology of flow patterns in vortex motions and turbulence. Applied Scientific Research. 53(3-4): 357-374.

[2] Moffatt H. K. 2001. Some remarks on topological fluid mechanics.An introduction to the geometry and topology of fluid flows. Springer, Dordrecht: 3-10.

[3] Lipinski D., Cardwell B. and Mohseni K. 2008. A Lagrangian analysis of a two-dimensional airfoil with vortex shedding. Journal of Physics A: Mathematical and Theoretical. 41(34): 344011.

[4] Rubenstein D., Yin W. and Frame, M. D. 2015. Biofluid mechanics: an introduction to fluid mechanics, macrocirculation, and microcirculation. Academic Press.

[5] Hadi M. I., Nazri M. and Abdullah A. 2020. Vortex formation in unsteady flow over NACA 4412 and NACA 4424 airfoils. ARPN J. Eng. Appl. Sci. 15(1): 27-33.

[6] Abdullah A., Roslan A. and Omar Z. 2018. Comparative study of turbulent incompressible flow past NACA airfoils. ARPN J. Eng. Appl. Sci. 13(21): 8527-8530.

[7] Abdullah A., Jafri M.N.S. M. and Zulkafli M. F. 2017. Numerical study of military airfoils design for compressible flow.ARPN J. Eng. Appl. Sci. 12(24): 7129-7133.

[8] Sofian M., Nurhayati R., RexcaA. J., SyarifulS. S. and Aslam A.2014. An evaluation of drag coefficient of wind turbine system installed on moving car. Applied Mechanics and Materials. 660: 689-693.

[9] Abdullah A., Kamsani M.A. and Abdullah K. 2017. Effect of ground proximity on the flow over STOL CH750 multi-element airfoil.IOP Conference Series: Materials Science and Engineering. 243(1): 1-7.

[10] Rashidi S., Hayatdavoodi M. and Esfahani J. A. 2016. Vortex shedding suppression and wake control: A review. Ocean Engineering. 126: 57-80.

[11] Kurtulus D. F. 2011. Introduction to micro air epts, design and applications. Feedback. 3: 5.

[12] Abdullah A., Yazi M. N., Ghafir M. F. A., Mohd S. and Rahim M. Z. 2017. Ground proximity effect on the flow over NACA 4412 multi-element airfoil in clean configuration. Journal of Physics: Conference Series. 914(1): 1-7.